Separation of the Longitudinal and Transverse Cross Sections in the $p(e,e'K^+)\Lambda$ and $p(e,e'K^+)\Sigma^0$ Reactions

R. M. Mohring[1], G. Niculescu[2], P. Gueye[2], D. Abbott[3], A. Ahmidouch[2,4], Ts. A. Amatuni[5], P. Ambrozewicz[6], T. Angelescu[7], C. S. Armstrong[8], J. A. Arrington[9], K. Assamagan[2], S. Avery[2], K. Bailey[9], K. Beard[2], S. Beedoe[10], E. Beise[1], H. Breuer[1], R. Carlini[3], J. Cha[2], C. C. Chang[1], N. Chant[1], E. Cisbani[12], G. Collins[1], W. Cummings[9], S. Danagoulian[10], R. De Leo[12], F. Duncan[1], J. Dunne[3], D. Dutta[13], T. Eden[2], R. Ent[3], L. Eyraud[14], L. Ewell[1], M. Finn[8], T. Fortune[15], V. Frolov[16], S. Frullani[12], C. Furget[14], F. Garibaldi[12], D. Gaskell[17], D. F. Geesaman[9], K. K. Gustafsson[1], J. -O. Hansen[9], M. Harvey[2], W. Hinton[2], E. Hungerford[18], M. Iodice[12], C. Jackson[10], C. Keppel[2,3], W. Kim[19], K. Kino[20], D. Koltenuk[15], S. Kox[14], L. Kramer[21,3], T. Leone[12], G. Lolos[12], A. Lung[1], D. Mack[3], R. Madey[2,4], M. Maeda[20], S. Majewski[3], P. Markowitz[21,3], C. J. Martoff[6], D. Meekins[8], A. Mihul[7], J. Mitchell[3], H. Mkrtchyan[5], S. Mtingwa[10], I. Niculescu[2], R. Perrino[12], D. Potterveld[9], J. W. Price[16], B. A. Raue[21,3], J.-S. Real[14], J. Reinhold[9], P. Roos[1], T. Saito[20], G. Savage[2], R. Sawafta[10], R. Segel[13], S. Stepanyan[5], P. Stoler[16], V. Tadevosian[5], L. Tang[2,3], L. Teodorescu[7], T. Terasawa[20], H. Tsubota[20], G. M. Urciuoli[12], J. Volmer[11], W. Vulcan[3], P. Welch[17], R. Williams[2], S. Wood[3], C. Yan[3], B. Zeidman[9]

[1] *University of Maryland, College Park, MD 20742, USA*
[2] *Hampton University, Hampton, VA 23668, USA*
[3] *Thomas Jefferson National Accelerator Facility, Newport News, VA 23606, USA*
[4] *Kent State University, Kent, OH 44242, USA*
[5] *Yerevan Physics Institute, Yerevan, Armenia*
[6] *Temple University, Philadelphia, PA 19122, USA*
[7] *Bucharest University, Bucharest, Romania*
[8] *College of William and Mary, Williamsburg, VA 23187, USA*
[9] *Argonne National Laboratory, Argonne IL 60439, USA*
[10] *North Carolina A & T State University, Greensboro NC 27411, USA*
[11] *Free University, Amsterdam, The Netherlands*
[12] *Physics Laboratory, Istituto Superiore di Sanitá and INFN-Sezione Sanitá, Rome, Italy*
[13] *Northwestern University, Evenston IL 60201, USA*
[14] *ISN, Grenoble, France*
[15] *University of Pennsylvania, Philadelphia PA 19104, USA*
[16] *Rensselaer Polytechnic Institute, Troy NY 12180, USA*
[17] *Oregon State University, Corvallis OR 97331, USA*
[18] *University of Houston, Houston, TX 77204, USA*
[19] *Kyungpook National University, Taegu, S. Korea*
[20] *Tohoku University, Sendai 982, Japan and*
[21] *Florida International University, Miami, FL 33199, USA*

(Dated: November 1, 2001)

We report measurements of cross sections for the reaction $p(e,e'K^+)$Y, for both the Λ and Σ^0 hyperon states, at the four-momentum transfers $0.5 < Q^2 < 2$ $(\mathrm{GeV/c})^2$, for three values of virtual photon polarization ϵ, allowing the decomposition of the cross sections into longitudinal and transverse components. The Λ data is a reanalysis of prior work, whereas the Σ^0 results have not been previously reported.

PACS numbers: 25.30.Rw, 13.40.Gp, 14.40.Aq

I. INTRODUCTION

Electromagnetic production of strange baryons has long been of interest because of the fact that such data can provide unique information about the flavor dependence of nucleon excited states. Unfortunately, progress in understanding the production mechanism has been slow, in no small part because of the lack of high quality data. With the recent availability of a high quality, continuous electron beam at Jefferson Laboratory, precise new measurements are now achievable over a wide kinematic range [1, 2].

In this paper, we present new cross section data on the reaction $p(e,e'K^+)\Sigma^0$ from Jefferson Lab experiment E93-018, that were acquired at values of the square of four-momentum transfer between the electron and the target, Q^2, between 0.5 and 2.0 $(\mathrm{GeV/c})^2$. At each value of Q^2, three different values of the virtual photon polarization ϵ were studied, allowing a separation of the cross section into its longitudinal and transverse components. Previously, comparable results on the Λ channel were reported [1]. However, in order to provide an internally consistent comparison between the two reaction channels, we also present a reanalysis of the Λ data. The primary difference in the analysis presented here and that of [1] is an improved determination of the the experimen-

tal acceptance, and the use of direct comparison to simulated yields in order to extract the cross section. The new analysis results in a significantly smaller longitudinal contribution and a weaker Q^2 dependence of the unseparated Λ cross section than was previously reported. After a brief introduction and a detailed description of the experiment and analysis, the data will be compared to isobaric models of meson electroproduction described below.

Exploratory measurements of kaon electroproduction were first carried out between 1972 and 1979 [3, 4]. In [3] the longitudinal and transverse contributions to the Λ and Σ^0 cross sections were separated for three values of Q^2. Two values of ϵ were measured for each kinematic setting with relatively poor statistical precision, and the uncertainties in the L/T separated results were large. In [4], the measurements were focused on pion electroproduction, but a sample of kaons was also acquired, from which cross sections were extracted. These measurements provided the first determination of the qualitative behavior of the kaon cross sections and were the basis for the development of modern models of meson electroproduction.

The theoretical models all attempt to reproduce the available data from both kaon production and radiative kaon capture, while maintaining consistency with SU(3) symmetry constraints on the coupling constants [5]. The energy regime addressed by these models is low enough that they are formulated using meson/nucleon degrees of freedom. However, they are explicitly constructed to yield the proper perturbative QCD (pQCD) results at higher energies [8]. The most recent theoretical efforts can be divided into two categories, isobaric models and those that use Regge trajectories.

The approach taken in the isobaric models is to explicitly calculate kaon production amplitudes from tree-level (*i.e.*, only one particle exchanged) processes. A typical selection of diagrams considered is depicted in Figure 1. For example, in David *et al.* [9], the authors sum over s-channel nucleon resonances up to and including spin 5/2, u-channel hyperon resonances of spin 1/2, and t-channel kaon resonances K*(892) and K1(1270). In the WJC model [5], a different selection of s and u channel resonances is included. Mart *et al.,* [6] include the lowest lying S- and P-wave resonances, plus an additional resonance D_{13} for which there appears to be evidence from kaon photoproduction [7].

The various isobaric models share the property that they initially include only spin 1/2 baryonic resonances (although the specific resonances differ) and determine the remaining coupling constants from performing phenomenological fits to the data. The coupling constants, which are the parameters of the theory, are not well-constrained due to the lack of available data. Because of this, one sees differences in the various models for quantities such as $g_{K\Lambda N}$. One issue that these differences reflect is that the various models disagree on the relative importance of the resonances entering the calculation. Further details on the various isobaric models can be found in [5, 9–11].

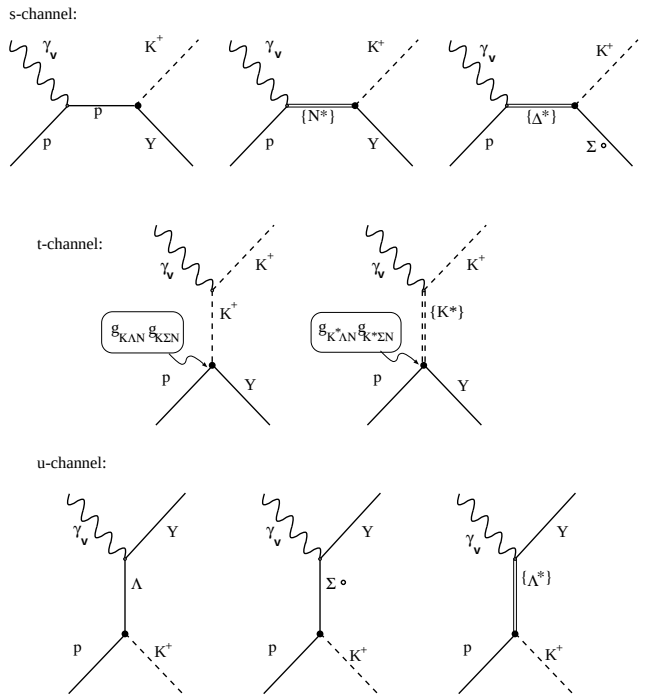

FIG. 1: Examples of Feynman diagrams for kaon electroproduction considered in the isobaric models. The couplings in the t-channel ($g_{K\Lambda N}$, etc...) are shown explicitly. Note that the s-channel processes involving Δ^* resonances are forbidden by isospin conservation for Λ production.

Models based on Regge trajectories [12] were developed in the early 1970's to describe pion photoproduction data, of which there is a relative abundance. This approach has recently been revisited by Vanderhaegen, Guidal, and Laget (VGL) [13]. Here, the standard single particle Feynman propagator, $1/(t-m^2)$, is replaced by a Regge propagator that accounts for the exchange of a family of particles with the same internal quantum numbers [14]. The extension of the photoproduction model to electroproduction is accomplished by multiplying the gauge invariant t-channel K and K* diagrams by a form factor (the isobaric models such as WJC also include electromagnetic form factors, however the functional forms used differ between models [5, 10]). For the VGL model this is given as a monopole form factor,

$$F_{K,K^*}(Q^2) = \frac{1}{1+Q^2/\Lambda^2_{K,K^*}} \ , \qquad (1)$$

where Λ^2_{K,K^*} are mass scales that are essentially free parameters, but can be fixed to fit the high Q^2 behavior of the separated electroproduction cross sections, σ_T and σ_L. For both the isobaric and Regge approaches, precise experimental results for longitudinal/transverse separated cross sections are important for placing constraints on the free parameters within the models that will give insight into the reaction mechanisms.

An additional motivation for performing measurements of L/T separated cross sections in kaon electroproduction is to determine the Q^2 dependence of the K^+ electromagnetic form factor. This can be accomplished through a measurement of the t-dependence of the longitudinal component of the cross section if it can be demonstrated that σ_L is dominated by photon absorption on a ground state kaon. This technique has been used to determine the π^+ electromagnetic form factor, including a recent new measurement [15]. While the kaon form factor cannot be extracted from the data presented here, it is the subject of future measurements at Jefferson Laboratory [16].

Finally, historically there has been interest in the ratio of Σ^0/Λ transverse cross sections, linked to contribution of sea quarks to nucleon structure [17, 18]. Within the context of the parton model, isospin arguments would lead one to expect the Σ^0/Λ transverse cross section ratio at forward kaon CM angles to approach 0 with increasing Bjorken x if the kaon production mechanism is dominated by the photon interacting with single valence u quark. When sea quarks are included in the nucleon's initial state, the approach to 0 is expected to be more rapid. Measurement of of $\sigma_T(\Sigma^0)/\sigma_T(\Lambda)$ over a broad range of x may provide information about the intrinsic $\overline{s}s$ content of the proton.

A. Elementary Kaon Electroproduction

The elementary kaon electroproduction reaction studied here,

$$\mathrm{e} + \mathrm{p} \rightarrow \mathrm{e}' + \mathrm{K}^+ + (\Lambda \text{ or } \Sigma^0) \ ,$$

is shown in Figure 2. An incident electron (e), scatters by radiating a virtual photon (γ_v). The scattered electron (e') travels at a polar angle θ_e in the Laboratory frame with respect to the direction of the incident beam, defining the scattering plane. The virtual photon carries momentum $\vec{q}$ and energy ν and interacts with a target proton to form a kaon (K^+) and a hyperon Y (here either a Λ or Σ^0). The kaon travels at a polar angle θ_{qK} in the Laboratory frame with respect to the virtual photon direction and is also detected. The reaction plane, defined by the produced kaon and produced hyperon, makes an angle ϕ with respect to the scattering plane.

The exclusive five-fold differential electroproduction cross section can be expressed in terms of a virtual photoproduction cross section, $\frac{d\sigma}{d\Omega^*_K}$, multiplied by a virtual photon flux factor, Γ_0 [19]. It is written in terms of the scattered electron energy, E', electron Lab frame solid angle, $d\Omega'_e \equiv d\cos\theta_e\, d\phi_e$, and kaon Center-of-Momentum frame (CM) solid angle, $d\Omega^*_K \equiv d\cos\theta^*_{qK}\, d\phi$ as

$$\frac{d^5\sigma}{dE' d\Omega'_e d\Omega^*_K} = \Gamma_0(E', \Omega'_e) \left(\frac{d\sigma}{d\Omega^*_K}\right) \ , \qquad (2)$$

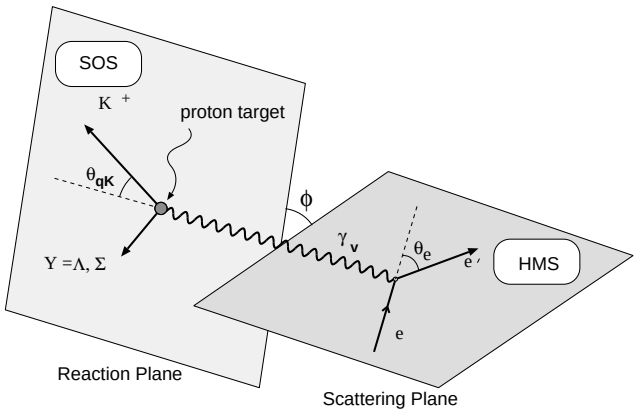

FIG. 2: Definition of the kaon electroproduction reaction. Note the azimuthal angle, ϕ, between the scattering and reaction planes with respect to the direction of the virtual photon.

with

$$\Gamma_0(E', \Omega'_e) = \frac{\alpha}{2\pi^2} \frac{(W^2 - m_p^2)}{2\, m_p} \frac{E'}{E} \frac{1}{Q^2} \frac{1}{(1-\epsilon)} \, . \qquad (3)$$

Note that the CM frame is that of the (virtual photon + proton) system, and that the CM frame counterparts to Lab variables will be denoted with an asterisk superscript. In this expression, α is the fine structure constant ($\approx 1/137$), m_p is the proton mass, W is the total CM energy of the (virtual photon + proton) system, Q^2 is the square of the four-momentum transfer carried by the virtual photon, and ϵ is the transverse linear polarization of the virtual photon, given by

$$\epsilon = \frac{1}{1 + 2\,\frac{|\mathbf{q}|^2}{Q^2}\,\tan(\frac{\theta_e}{2})} \ , \qquad (4)$$

where $\mathbf{q}$ is the virtual photon three-momentum.

Rather than use Equation 2, the form of the virtual photoproduction cross section used for this analysis is

$$\frac{d^5\sigma}{dQ^2 dW\, d\phi_e d\Omega^*_K} = \Gamma(Q^2, W) \left(\frac{d\sigma}{d\Omega^*_K}\right) \ , \qquad (5)$$

where the transformation between the spaces $(E', \Omega'_e) \leftrightarrow (Q^2, W)$ is incorporated into the virtual photon flux, Γ, via

$$\Gamma(Q^2, W) \ = \ \Gamma_0(E', \Omega'_e) \times \frac{W}{2 m_p\, E\, E'} \qquad (6)$$

$$= \ \frac{\alpha}{4\pi^2} \frac{(W^2 - m_p^2)}{2\, m_p^2\, E^2} \frac{W}{Q^2} \frac{1}{(1-\epsilon)} \, . \qquad (7)$$

Because none of the incoming or outgoing polarizations of the particles involved were measured, the virtual photoproduction cross section can be decomposed into four terms:

$$\frac{d\sigma}{d\Omega^*_K} = \sigma_T + \epsilon\, \sigma_L + \sqrt{2\epsilon(\epsilon+1)}\, \sigma_{LT} \cos\phi + \epsilon\, \sigma_{TT} \cos 2\phi \ , \qquad (8)$$

No.	$\langle Q^2 \rangle$ $(\mathrm{GeV/c})^2$	$\langle W \rangle$ GeV	$\langle \epsilon \rangle$ (for Λ)	E GeV	$\mathrm{P_{HMS}}$ GeV/c	θ_{HMS} deg	$\mathrm{P_{SOS}}$ GeV/c	θ_{SOS} deg
1	0.52	1.84	0.552	2.445	0.833	29.27°	1.126	13.40°
2	0.52	1.84	0.771	3.245	1.633	18.03°	1.126	16.62°
3	0.52	1.84	0.865	4.045	2.433	13.20°	1.126	18.34°
4	0.75	1.84	0.462	2.445	0.725	37.95°	1.188	13.42°
5	0.75	1.84	0.724	3.245	1.526	22.44°	1.188	17.62°
6	0.75	1.84	0.834	4.045	2.326	16.23°	1.188	19.75°
7	1.00	1.81	0.380	2.445	0.635	47.30°	1.216	13.40°
8	1.00	1.81	0.678	3.245	1.435	26.80°	1.216	18.20°
9	1.00	1.81	0.810	4.045	2.236	19.14°	1.216	20.78°
10	2.00	1.84	0.363	3.245	0.844	50.59°	1.634	13.42°
11	2.00	1.84	0.476	3.545	1.145	41.11°	1.634	15.67°
12	2.00	1.84	0.613	4.045	1.645	31.83°	1.634	18.14°

TABLE I: Kinematical settings measured in E93-018. Note that there are three settings of the virtual photon polarization, ϵ, for each of four values of Q^2. Data were taken in the Λ and Σ^0 channels simultaneously. For ease of discussion, the settings have been labeled as Point 1 through Point 12 in increasing order of Q^2, and with increasing order of ϵ within each Q^2 setting.

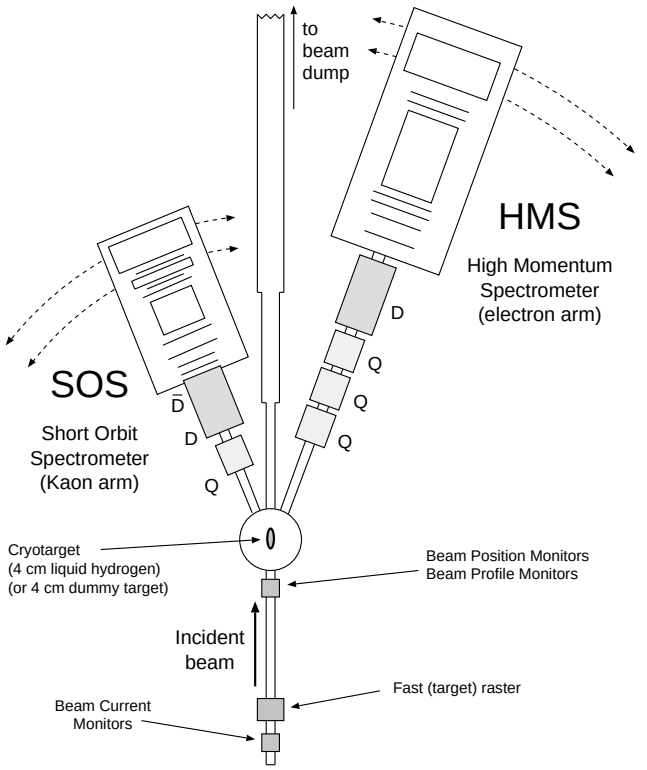

FIG. 3: Schematic top view of Hall C spectrometer setup showing the location of the HMS and SOS relative to the target and incident beam.

where σ_T is the cross section due to transversely polarized virtual photons, σ_L is due to longitudinally polarized virtual photons, and σ_{LT} and σ_{TT} are interference terms between two different polarization states. If one integrates the cross section over all $\phi \in (0, 2\pi)$, the interference terms vanish leaving only the combined contributions from the transverse and longitudinal cross sections, $\sigma_T + \epsilon\sigma_L$. By measuring the cross section at several values of the virtual photon polarization, ϵ, the cross sections σ_T and σ_L can be separated. The experimental setup described here was such that at each of the four values of Q^2, the full range in $\phi \in (0, 2\pi)$ was accessible at three different values of the virtual photon polarization, ϵ, as listed in Table I. The data were fitted using the linear dependence between $(\sigma_T + \epsilon\sigma_L)$ and ϵ. The intercept and slope of the fitted line were used to extract σ_T and σ_L for each Q^2, for both the Λ and Σ^0 channels.

II. EXPERIMENTAL APPARATUS

Data acquisition for experiment E93-018 took place in the Hall C experimental area of Jefferson Lab in 1996. A schematic top view showing the relation between the spectrometers and the beamline/target chamber is depicted in Figure 3. The Continuous Wave (CW, 100% duty factor) electron beam consisted of 1.67 ps micropulses spaced approximately 2 ns apart arising from the 499 MHz RF structure of the accelerator, with beam energies between 2.4 and 4 GeV. The primary target was a (4.36 ± 0.01) cm long liquid hydrogen cryotarget with 0.01 cm aluminum end windows. Background from the end windows, always less than a few percent, was measured (and subtracted) using an aluminum target with an equivalent radiator thickness as the hydrogen. The integrated beam current (10-40 μA) was measured to an accuracy of 1.5% using a pair of microwave cavities calibrated with a DC current transformer. In order to avoid target density fluctuations arising from beam heating, the beam was rastered in a 1×1 mm^2 square pattern at the entrance to the target.

The scattered electrons were detected in the High Momentum Spectrometer (HMS), consisting of three superconducting quadrupole magnets in sequence followed by a superconducting dipole, followed by a detector package situated near the focal plane of the optical system. The electroproduced kaons were detected in the Short Orbit Spectrometer (SOS). The SOS is a non-superconducting magnetic spectrometer with one quadrupole (Q) magnet followed by two dipoles (D and $\overline{\mathrm{D}}$) which share a common yoke. It was designed with a short flight path in order to allow for detection of unstable, short-lived particles, such as kaons or pions, with good efficiency. Selected properties of the two spectrometers are listed in Table II.

Both spectrometers were equipped with multiwire drift chambers for particle tracking and segmented scintillator hodoscope arrays for time-of-flight (TOF) measurement and trigger formation. Additionally, the HMS

	HMS	SOS
Maximum central momentum	7.5 GeV/c	1.75 GeV/c
Momentum acceptance	±10 %	±20 %
Ang. Acceptance (in-plane)	±28 mrad	±65 mrad
Ang. Acceptance (out-of-plane)	±70 mrad	±40 mrad
Solid Angle (4.36 cm LH_2 target)	6.5 msr	6.5 msr
Minimum central angle (E93-018)	13.2°	13.4°
Optical length	26.0 m	7.4 m

TABLE II: Selected properties of the HMS and SOS.

utilized a combination of a gas-filled threshold Čerenkov detector and a lead-glass calorimeter for e/π^- separation, while the SOS had a diffusely-reflecting aerogel threshold Čerenkov detector ($n = 1.034$) for the purposes of K^+/π^+ separation. A lucite Čerenkov detector was also in the detector stack, but was not used in the present analysis with the exception of accounting for the energy loss of the kaons passing through the detector. Detection efficiencies in both spectrometers were dominated by the track reconstruction efficiency, with additonal small losses due to the coincidence circuit and the data acquisition dead time (see Table III.)

III. DATA ANALYSIS

The raw data were processed and combined with additional experimental information such as the momentum and angle settings of the spectrometers, detector positions, and beam energy to yield particle trajectories, momenta, velocities, energy deposition, and to perform particle identification. Physics variables (such as Q^2, W, θ_e, $\mathbf{p_K}$, θ_{qK}...) were determined for each event at the interaction vertex, and then yields of electroproduced kaons as a function of a given subset of these variables were calculated.

A. Kaon Identification

In each spectrometer, the velocities of the detected particles were calculated using the timing information from the scintillator hodoscopes. For the SOS, two additional software cuts were implemented to select kaons out of the proton and pion backgrounds: a cut on the velocity as measured from TOF information (called $\beta_{\rm tof}$), and a cut on the number of photoelectrons detected in the aerogel Čerenkov detector.

The cut on $\beta_{\rm tof}$ was implemented as a cut on the quantity $(\beta_{\rm tof} - \beta_{\rm K})$, where $\beta_{\rm K}$ is the velocity of the detected hadron as determined from the measured momentum under the assumption that the incident particle was a kaon, defined as:

$$\beta_{\rm K} \equiv \frac{|\mathbf{p}|}{E} = \frac{|\mathbf{p}|}{\sqrt{|\mathbf{p}|^2 + m_K^2}}. \qquad (9)$$

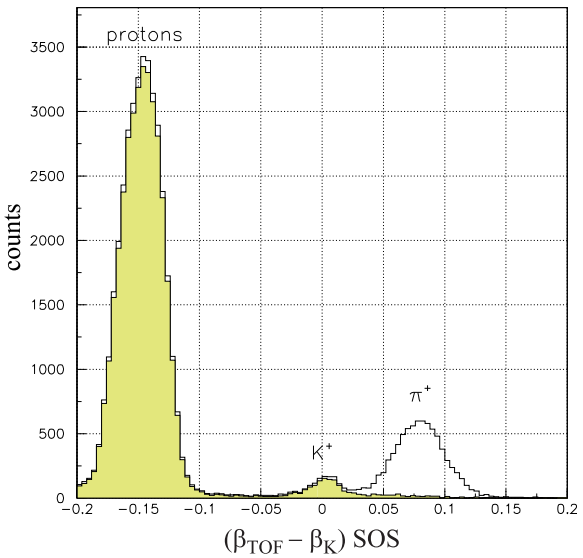

FIG. 4: A typical $\beta_{\rm tof} - \beta_{\rm K}$ spectrum for the SOS, shown with (shaded) and without (unshaded) a software aerogel cut.

The unshaded spectrum in Figure 4 shows the quantity $(\beta_{\rm tof} - \beta_{\rm K})$. In the analysis, a cut was placed at $|\ (\beta_{\rm tof} - \beta_{\rm K})\ | < 0.04$, which eliminated essentially all protons, and a significant fraction of pions.

The second cut was on the number of photoelectrons detected in the aerogel Čerenkov. This eliminated the majority of the remaining background pions that the $(\beta_{\rm tof} - \beta_{\rm K})$ cut did not reject. The (very few) pions that survived both of these cuts were eliminated by the subtraction of the random background (see next section). The shaded region in Figure 4 shows what remains after applying a cut requiring less than 3.5 photoelectrons in the aerogel detector.

B. Coincidence Cuts

The relative timing between the HMS and SOS signals was used to identify true kaon-electron coincidences. This coincidence time was corrected to account for variations in flight time arising from variations in particle velocity and path length through the spectrometers. An arbitrary offset was added such that events in which the electron and kaon originated from the same beam bunch would have a time of 0 ns. Figure III B shows $(\beta_{\rm tof} - \beta_{\rm K})$ for the SOS plotted versus the corrected coincidence time for a single run, without having applied the kaon identification cuts. Three horizontal bands of electron coincidences with protons, kaons, and pions are

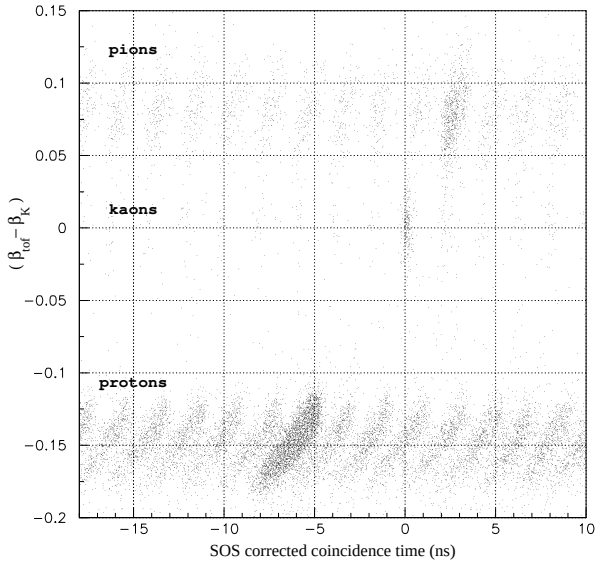

FIG. 5: Plot of $(\beta_{\rm tof}-\beta_{\rm K})$ vs. SOS corrected coincidence time. Visible are three horizontal bands corresponding to protons, kaons, and pions. The coincidence time is offset such that the in-time kaons appear at 0 ns. See text for further details.

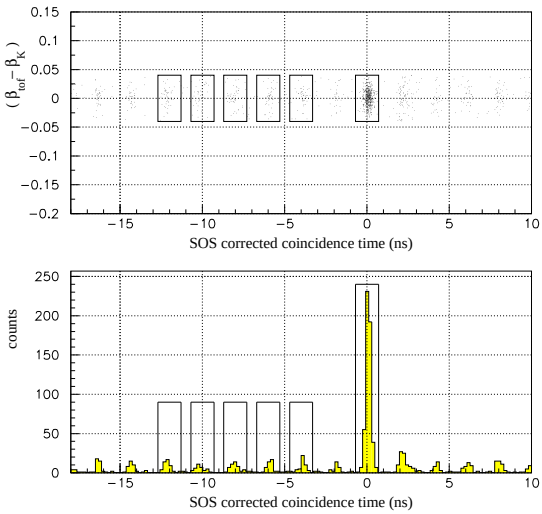

FIG. 6: The upper panel shows $(\beta_{\rm tof}-\beta_{\rm K})$ vs. SOS corrected coincidence time, after applying cuts on $(\beta_{\rm tof}-\beta_{\rm K})$ and the aerogel. The single boxed region to the right is the in-time peak, and the five boxed regions to the left contain random coincidences. The lower panel shows the one-dimensional spectrum of SOS corrected coincidence times corresponding to the upper panel.

clearly identified, with the in-time pion and proton peaks offset from the in-time kaon peak by at least one beam bunch. Random coincidences, resulting from an electron and hadron from different beam bunches, have a coincidence time that is offset from the in-time peak by a multiple of ∼2 ns.

After applying the $(\beta_{\rm tof}-\beta_{\rm K})$ and aerogel cuts, the distribution shown in figure III B reduces to that shown in Figure III B(a). In Figure III B(b) the one-dimensional projection of the upper half is shown. The in-time peak dominates over the purely random coincidences. The data were cut on the coincidence time around the peak, at $|\,{\rm cointime(SOS)}\,| < 0.65$ ns. The random background was estimated by averaging over five bunches to the left of the in-time peak, and then subtracting it the in-time yield to give the true kaon electroproduction yield.

C. Missing Mass Reconstruction

Once true e-K coincidences were identified, the missing mass, m_Y, of the produced hyperon was reconstructed from measured quantities as

$$m_Y^2 = -Q^2+m_K^2+2\,\nu\,m_p-2\,E_K(\nu+m_p)-2\,\mathbf{q}\cdot\mathbf{p_K}\ , \quad (10)$$

where $(E_K, \mathbf{p_K})$ is the kaon four-vector, and $(\nu, \mathbf{q})$ is the virtual photon four-vector.

Figure 7 is a histogram of the calculated missing mass, showing peaks at the Λ and Σ^0 masses. The tails

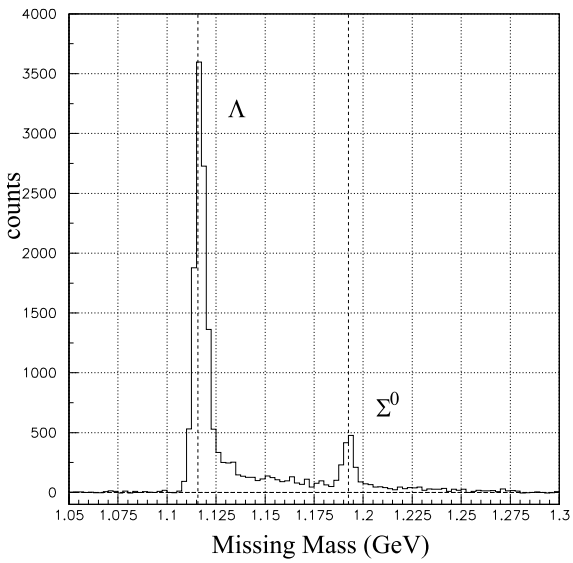

FIG. 7: An example of a missing mass spectrum for $\rm p(e,e'K^+)Y$ showing the Λ and Σ^0 peaks and radiative tails. The vertical dashed lines are located at the accepted Λ and Σ^0 masses. Note that this spectrum has already been corrected for random and target endcap yields.

sloping off toward higher missing mass from each of these peaks are due to the effects of radiative processes. A cut of $(1.100 < m_Y < 1.155)$ GeV was used to identify events with a Λ in the final state, and $(1.180 < m_Y < 1.230)$ was used for the Σ^0 final state. In each case, the yield was then corrected for the fraction of events outside of the window as a result of radiative processes. The Σ^0 analysis also required subtraction of the Λ events in the radiative tail under the Σ^0 peak. After application of all cuts and identification of true $p(e,e'K^+)Y$ events, the measured yields were corrected for losses due to detection efficiencies (such as electronic and computer live time, aerogel cut efficiency, tracking efficiency), kaon decay, and kaon absorption through the target and spectrometer materials. A summary of these corrections and their associated errors can be found in Table III.

One of the largest corrections arose from the fact that kaons are unstable and have a short mean lifetime. As a result, a large fraction of the kaons created at the target decay into secondary particles before they can be detected. The survival fraction of the detected kaons is

$$\frac{N_{\rm detected}}{N_{\rm at\,target}} = e^{-\left(\frac{m_K\, d}{p_K\, \tau}\right)}\,, \qquad (11)$$

where d is the distance traveled to the detector and $\tau \approx 12.4$ ns ($c\tau \approx 3.713$ m) is the mean lifetime of a kaon at rest [20]. The survival fraction varied between 0.3 and 0.5 for the range of kaon momenta detected here. Although the mean kaon decay correction is large, its uncertainty is small because both the kaon's trajectory length and momentum were accurately determined by the SOS tracking algorithm. An additional few percent correction was applied to account for the possibility that the decay products might actually be detected, mimicking an otherwise lost kaon event. This correction was estimated through the use of a Monte Carlo simulation of the six most likely decay processes as listed in [20]. Further details regarding the data analysis can be found in [21].

Property	Typical Correction	Random Error	Scale Error
HMS Acceptance	—	—	2.0 %
SOS Acceptance	—	—	2.0 %
Cut variation (Q^2, etc...)	—	0.7 - 3.1 %	—
Scaling function	0.9 - 1.1	0.5 %	2.0 %
Radiative Correction	—	1.0 %	1.0 %
Cut variation (m_Y)	—	0.5 %	—
Acceptance × Rad Corr	1.2 - 1.4		
HMS Tracking eff.	0.91 - 0.98	0.5 %	—
SOS Tracking eff.	0.83 - 0.93	1.0 %	—
HMS Trigger eff.	1.0	0.1 %	—
SOS Trigger eff.	1.0	0.1 %	—
Coincidence eff.	0.950 - 0.985	0.5 %	—
TOF $\beta = 0$	0.96 - 0.99	0.5 %	—
HMS Electr. Live Time	0.996 - 1.000	0.1 %	—
SOS Electr. Live Time	0.973 - 0.990	0.1 %	—
Computer Live Time	0.91 - 1.00	0.3 %	—
Cointime cut eff.	≈ 1.0	0.1 %	—
TOF β cut eff.	> 0.99	0.5 %	—
HMS Čerenkov eff.	≈ 0.998	0.2 %	—
Aerogel cut ineff.	0.974	—	0.3 %
Kaon Absorption	0.94 - 0.97	0.5 %	0.5 %
Kaon Decay	2.5 - 4.0	1.0 %	3.0 %
Decay Prod. K^+ Mimic	0.990 - 0.995	0.5 %	—
Target Length/Density	—	—	0.4 %
Target Density Fluct.	0.992	0.4 %	—
Target Purity	0.998	—	0.2 %
Charge Measurement	—	—	1.5 %
Random Subtraction	2% to 5%	0.5 %	—
Endcap Subtraction	1 - 2% Λ 4 - 8% Σ^0	0.5 %	—
Total		2.5 - 3.9 %	5.0 %

TABLE III: Systematic corrections and errors in the E93-018 analysis.

IV. MONTE CARLO SIMULATION

In order to extract cross section information from the data, a detailed Monte Carlo simulation of the experiment was developed that modeled the optical properties of both spectrometers, multiple scattering, energy loss from passage through materials, kaon decay, and radiative processes. The simulation code used for this analysis was largely based on that developed in ref. [22], which uses the Plane Wave Impulse Approximation (PWIA) to model A(e,e′p) for various nuclei, incorporating radiative corrections. In order to test the validity of the Monte Carlo, elastic scattering (e,e′) and (e,e′p) data were taken and compared with the simulation. The code was then modified to simulate kaon electroproduction from hydrogen. Note that as a matter of convention in the discussions that follow, the term "data" always refers to the measured experimental data yields, and the term "MC" always refers to the simulated events and yields.

A. Event Generation

In the MC event generator, a random target interaction point is selected, consistent with the target length and raster amplitudes. The beam energy is then chosen about a central (input) value with a resolution $dE/E = \pm 0.5\%$. The quantities $(Q^2, W, \phi_e, \theta^*_{q_K}, \phi)$ are randomly generated for each event, with unit cross section in the phase space $\Delta V^5_{\rm gen} \equiv \Delta Q^2 \Delta W \Delta\phi_e \Delta\Omega^*_K$ and with limits that extend well beyond the physical acceptances of the spectrometers.

With the scattered electron quantities (Q^2, W, ϕ_e) generated (and after the effects of radiative corrections are considered) the laboratory frame virtual photon four-vector q^μ, and its counterpart $(q^\mu)^*$ defined in the CM frame of the virtual photon and proton, are completely specified.

For the kaon side, the hyperon $Y = (\Lambda, \Sigma^0)$ being generated is specified in the Monte Carlo input file. Because the kaon-hyperon production is a two-body reaction, the momentum of the outgoing kaon in the CM frame is fixed by knowledge of W as

$$|\mathbf{p}^*_{\mathbf{K}}| = \sqrt{\left(\frac{(W^2 + m_K^2 - m_Y^2)}{2\,W}\right)^2 - m_K^2}\ . \qquad (12)$$

The remaining components of the kaon four-vector in the CM frame, $(p^\mu_K)^*$, are determined using the quantities (θ^*_{qK}, ϕ). Then, the kaon is Lorentz boosted back to the lab frame in a coordinate system in which the z-axis is along the $\mathbf{q}$ vector. Finally, a coordinate rotation is performed to yield the "spectrometer" values of momentum and angles of the kaon at the interaction vertex (referred to as "vertex quantities").

The radiative correction routines supplied in the original $(e, e'p)$ code of ref. [22] were based on the work of Mo and Tsai [23], extended to be valid for a coincidence framework. Details of the corrections are well-documented in several references [22, 24, 25]. The procedure outlined in these references was implemented for quasielastic proton knockout. In the present work, the same procedure was used with two modifications to consider kaon production: the mass of the outgoing particle was changed to m_K and the vertex reactions were modified to follow a parameterization of the kaon cross section (discussed below).

Figure 8 shows the cross section weighted MC calculation of the radiative tail (solid line) plotted on top of the measured data (crosses), on both linear and logarithmic scales. Although the resolution of the MC peak is slightly narrower than that of the data (a result of the spectrometer model), overall the agreement between the MC and data is quite good. The missing mass cut used to define the Λ ($1.100 < m_Y < 1.155$ GeV) was sufficiently wide that the extracted cross section was insensitive at the level of 0.5% to variations in the cut.

Figure 9 shows the sequential effect of placing the cuts on the experimental data from a single run. In the analysis, all of the cuts were systematically varied and their effects on the cross section noted. The standard deviation of the resulting cross sections was used as an estimate of the systematic error on the quoted cross section due to each cut.

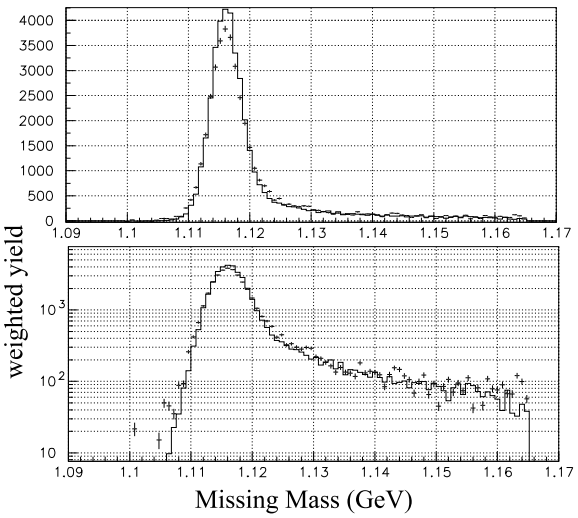

FIG. 8: Yield spectrum of missing mass comparing MC (solid line) to data (crosses) for p(e,e′K$^+$)Λ, on both linear (top panel) and logarithmic (bottom panel) scales, normalized by the extracted cross section.

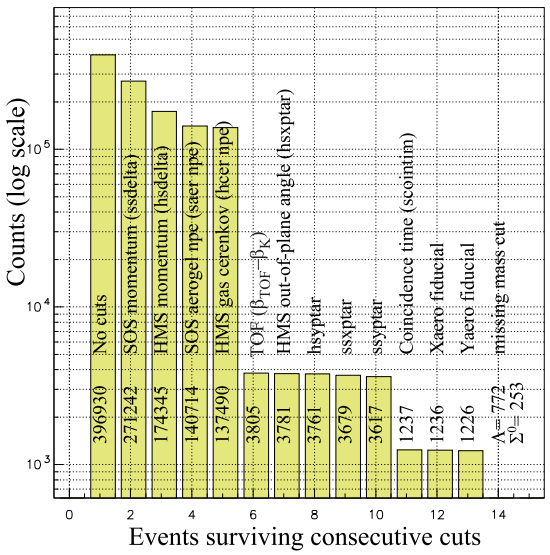

FIG. 9: Histogram showing the cumulative effects of applying the cuts (note logarithmic scale). Shown are the number of counts surviving after applying the cuts as indicated from left to right, resulting in a final yield of 772 Λ and 253 Σ^0.

B. Equivalent Monte Carlo Yield

The equivalent experimental yield given by the MC can be expressed as

$$Y_{\rm MC} = L_{\scriptscriptstyle H} \times \int \left[\frac{d^5\sigma}{dQ^2 dW\, d\phi_e d\Omega^*_{\scriptscriptstyle K}} \right] \times A(d^5V)\, R(d^5V)\, dQ^2 dW\, d\phi_e d\Omega^*_{\scriptscriptstyle K}\,, \quad (13)$$

where $L_{\scriptscriptstyle H}$ is the experimental luminosity, A is the acceptance function of the coincidence spectrometer setup, and R is the radiative correction. The experimental luminosity is given by

$$L_{\scriptscriptstyle H} = C_{\rm eff}\, N_{\rm beam}\, N_{\rm tgt}\,, \quad (14)$$

where $C_{\rm eff}$ is a multiplicative factor containing all the global experimental efficiencies (such as the tracking efficiency, dead times, etc.), and $N_{\rm beam}$ and $N_{\rm tgt}$ are the number of incident electrons and the number of target nucleons/cm^2, respectively.

Substituting the virtual photoproduction cross section (Eq. 5) for the full electroproduction relation results in

$$Y_{\rm MC} = L_{\scriptscriptstyle H} \times \int \left[\Gamma(Q^2, W) \left(\frac{d^2\sigma}{d\Omega^*_{\scriptscriptstyle K}} \right) \right] \times A(d^5V)\, R(d^5V)\, dQ^2 dW\, d\phi_e d\Omega^*_{\scriptscriptstyle K}. \quad (15)$$

In order to eventually extract cross sections by comparison with data, the MC yield was weighted by a single global factor σ_0, representing the cross section at a fixed value of $(\langle Q^2\rangle, \langle W\rangle)$ and $\theta^*_{qK} = 0^\circ$. The event-by-event variation of the cross section within the experimental acceptance was modeled using previously existing data. This procedure is equivalent to replacing the cross section in equation 15 by

$$\left(\frac{d\sigma}{d\Omega^*_{\scriptscriptstyle K}} \right) = \left(\frac{d\sigma}{d\Omega^*_{\scriptscriptstyle K}} \right)\Bigg|_{(\langle Q^2\rangle, \langle W\rangle, \theta^*_{qK} = 0^\circ)} \times \left[\frac{f(Q^2, W, \theta^*_{qK})}{f(\langle Q^2\rangle, \langle W\rangle, \theta^*_{qK} = 0^\circ)} \right] \equiv \sigma_0 \frac{f}{\langle f\rangle}\,. \quad (16)$$

where the scaling function $f/\langle f\rangle$ describes the behavior of the cross section across the acceptance. The resulting extracted cross section is not very sensitive to the choice of scaling functions because the cross section does not vary strongly in Q^2, W, and θ^*_{qK} within the acceptance. Inserting equation 16 into equation 15 gives the expression

$$Y_{\rm MC} = L_{\scriptscriptstyle H} \times \sigma_0 \times \int \left[\Gamma(Q^2, W) \left(\frac{f}{\langle f\rangle} \right) \right] \times A(d^5V)\, R(d^5V)\, dQ^2 dW\, d\phi_e d\Omega^*_{\scriptscriptstyle K}\,. \quad (17)$$

The integral is evaluated numerically via the Monte Carlo simulation, with each Monte Carlo event being appropriately weighted with the radiative corrections, virtual photon flux, and scaling function. The influence of the acceptance function, A, arises through the fraction of generated events that successfully traverse the spectrometers and are reconstructed. The MC equivalent yield then reduces to

$$Y_{\rm MC} = L_{\scriptscriptstyle H} \times \sigma_0 \times \Delta^5 V_{\rm gen} \times \left(\frac{(\text{Number of MC successes})_{\rm weighted}}{\text{Number of MC tries}} \right). \quad (18)$$

Finally, by setting the equivalent yields of MC and measured data to be equal (i.e., $Y_{\rm MC} = Y_{\rm DATA}$), the cross section σ_0 at the scaling point is extracted.

C. Scaling Functions

The previously existing world data were used to account for the cross section behavior across the acceptance. In Bebek *et al.* [3], the behavior of the cross section is parameterized as:

$$\frac{d\sigma}{d\Omega^*_{\scriptscriptstyle K}} \sim f_{\rm Bebek}(Q^2) \times f_{\rm Bebek}(W)\,, \quad (19)$$

where

$$f_{\rm Bebek}(Q^2) = \frac{1}{(Q^2 + X)^2} \quad (20)$$

with $X = 2.67$ for the Λ channel, and $X = 0.79$ for the Σ^0, and

$$f_{\rm Bebek}(W) = \frac{|\mathbf{p}^*_{\mathbf{K}}|}{W(W^2 - m_p^2)}. \quad (21)$$

In a recent analysis of another set of electrokaon production data [26], it was shown that data at values of W near the production threshold for the Λ cross section were not accurately reproduced by the W dependence in Eq. 21. In that analysis, a function of the following form was proposed, motivated by the hypothesis that there are possible resonance contributions to the cross section at lower W:

$$f(W) = \frac{C_1\ |\mathbf{p}^*_{\mathbf{K}}|}{W(W^2 - m_p^2)} + \frac{C_2\ A^2\, B^2}{(W^2 - A^2)^2 + A^2 B^2} \quad (22)$$

with $A = 1.72$ GeV, $B = 0.10$ GeV, $C_1 = 4023.9$ GeV^2 nb/sr, and $C_2 = 180.0$ GeV^2 nb/sr. This modified form was used here to scale in W, while Eq. 20 was used to scale in Q^2.

The θ^*_{qK} behavior was estimated using the results of Brauel, *et al.* [4]:

$$2\pi \frac{d^2\sigma}{dt d\phi} \sim e^{-\xi|t|}\,, \quad (23)$$

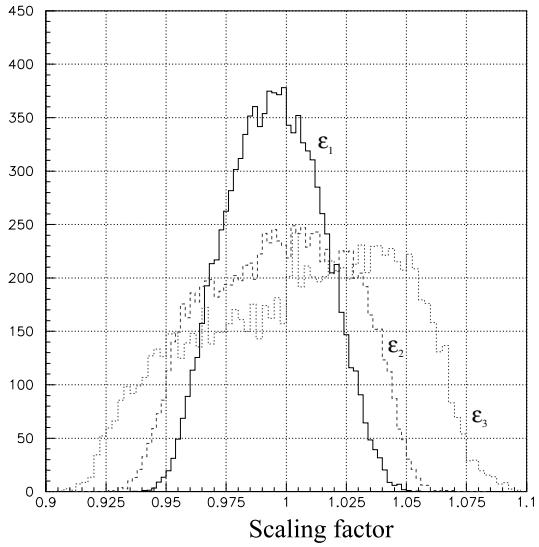

FIG. 10: The magnitude of the MC scaling factor $f/\langle f\rangle$ for the three values of ϵ at $Q^2 = 0.52$ (GeV/c)^2 (Points 1, 2, and 3).

where $\xi = 2.1$ for the Λ, and $\xi = 1.0$ for the Σ^0, with the Mandelstam variable t defined as

$$-t = -Q^2 + m_K^2 - 2\,E_K^*\nu^* + 2\,|\mathbf{q}^*||\mathbf{p}_\mathbf{K}^*|\cos\theta_{qK}^* \ , \quad (24)$$

where $(E_K^*, \mathbf{p}_\mathbf{K}^*)$ is the kaon four-vector in the CM frame, and $(\nu^*, \mathbf{q}^*)$ is the virtual photon four-vector in the CM frame. It can be shown that the behavior of the cross section as a function of θ_{qK}^* for fixed Q^2 and W can be expressed as

$$\frac{d\sigma}{d\Omega_K^*} \sim f(\theta_{qK}^*) = f(t) = \frac{1}{2\pi}\, e^{-\xi|t|}\,(-2|\mathbf{q}^*||\mathbf{p}_\mathbf{K}^*|) \ . \quad (25)$$

At $\theta_{qK}^* = 0^\circ$, the variable $(-t)$ becomes $(-t_{min})$ given by

$$-t_{min} = -Q^2 + m_K^2 - 2\,E_K^*\nu^* + 2\,|\mathbf{q}^*||\mathbf{p}_\mathbf{K}^*| \ , \quad (26)$$

resulting in a scaling behavior of

$$\frac{f(\theta_{qK}^*)}{\langle f(\theta_{qK}^* = 0^\circ)\rangle} = \frac{e^{-\xi|t|}}{e^{-\xi|t_{min}|}} = e^{-\xi(|t|-|t_{min}|)} \ . \quad (27)$$

Note that $-t_{min}$ is a function of Q^2 and W through its dependence on ν^*.

In order to extract cross sections at the specific value of $\theta_{qK}^* = 0^\circ$, each event in the MC was also not only weighted by the Q^2 and W scaling functions (defined in Eqs. 20 and 22), but also scaled to $t_{min}(Q^2, W)$ using Eq. 27.

Figure 10 shows a histogram of the distribution of magnitudes of the scaling factor $f/\langle f\rangle$ (i.e., the product of all scaling factors in Q^2, W, and θ_{qK}^*) applied to the MC data on an event-by-event basis corresponding to the three values of ϵ at the $Q^2 = 0.52$ (GeV/c)^2 setting. The spread in values of the scaling factor is largest at this lowest Q^2, and is essentially always less than $\pm 8\%$. The dependence of the extracted cross section on the form of $f/\langle f\rangle$ was investigated in depth and the maximum observed effect was 2.3%.

V. RESULTS

Cross sections were extracted by forcing the ratio of data to MC yields to be unity through adjustment of the single overall normalization factor σ_0 in the MC. After a first pass through the analysis, both the data and MC yields were stored in (typically 12) bins of ϕ. The ratio of data/MC was calculated in each bin yielding a zeroth order cross section for that bin. The procedure was then iterated, applying the extracted $(n-1)^{th}$ order cross section as a weighting factor for the yields in each ϕ bin using the generated values of the MC ϕ as the bin index. Typically the extracted cross section stabilized to within 0.1% of its value in three iterations. These final bin-by-bin values were fitted to a constant plus a harmonic ϕ dependent function of the form $A + B\cos\phi + C\cos 2\phi$ in order to extract $A = \sigma_T + \epsilon\sigma_L$. Varying the number of ϕ bins used to carry out the fit left the extracted cross section unchanged to better than 0.5%. Note that with a single ϕ bin, the ϕ dependence naturally cancels because the ϕ acceptance is uniform, provided one restricts the accepted events to values of θ_{qK}^* less than 10°. The ϕ dependence of the cross section, while apparently nonzero, could not be extracted quantitatively due to the low statistics per bin and poor ϕ reconstruction resolution.

The procedure for extracting the Σ^0 cross section was similar to that for the Λ, except that the Σ^0 yield was also corrected for the Λ radiative tail beneath the Σ^0 peak in the missing mass spectrum. The Λ-specific MC was used to determine the number of background Λ counts that were within Σ^0 cuts. The Λ-specific MC was weighted with the extracted Λ cross section, binned in the same manner as the data, and was subtracted from each data bin. The upper half of Figure 11 shows the combination of the Λ-specific and Σ^0-specific MC simulations plotted on top of the data missing mass. The lower half of the figure shows the remaining Σ^0 data after subtracting the Λ-specific MC, with the Σ^0-specific MC superimposed. Varying the Λ cross section in the Σ^0 extraction analysis by $\pm 10\%$ resulted in changes of less than 2% in the Σ^0 cross section. An additional scale uncertainty proportional to the Λ cross section uncertainty was thus applied to the Σ^0 results.

Typical values for all corrections to the data and/or the MC, along with the resulting systematic errors in the cross section, are shown in Table III. The statistical errors for the various settings ranged from $1.0-3.1\%$ for the Λ, and from $4.8-5.9\%$ for the Σ^0. The systematic errors are broken down into "random" and "scale" errors. Since random errors affect each kinematic

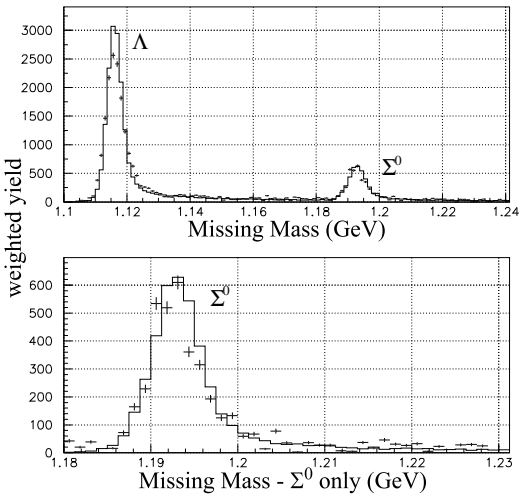

FIG. 11: Use of the MC to correct for the Λ radiative tail below the Σ^0 missing mass peak. The upper panel shows the combination of the Λ-specific and Σ^0-specific MC simulations (solid histogram) plotted on top of the data missing mass (crosses). The lower panel shows the remaining Σ^0 data after subtracting the Λ-specific MC, with the Σ^0-specific MC superimposed. The MC is normalized using the extracted Λ and Σ^0 cross sections.

setting in an independent manner, they were retained for the linear fit of the L/T separation while the global errors that result in an overall multiplicative factor to the data were ignored for the fitting procedure. The sources of the errors in Table III are discussed in detail in [21].

A. Λ and Σ^0 cross sections

The extracted p(e,e′K$^+$)Λ and p(e,e′K$^+$)Σ^0 unseparated cross sections are given in Table IV. For the sake of comparison, the unseparated cross sections at the highest ϵ values (which were similar to those of the earlier data) are also shown in figures 12 and 13 along with the previous world data taken from [27, 28] (also, see [21]). For the purposes of this plot, the E93-018 results have been scaled to $\langle W\rangle = 2.15$ GeV using the parameterization in [3] (Equation 21) and include a 5% (6%) scale error for the Λ (Σ^0) data. The previous world data shown in this plot have been scaled to ($\langle W\rangle = 2.15$ GeV, $\theta^*_{qK} = 0^\circ$), using equations 21 and 27. It should be noted that this comparison is not appropriate if one wants to extract a quantitative global Q^2 dependence of the cross section since the data shown are at varying values of t, ranging from 0.05-3.0. Nonetheless, qualitatively good agreement is seen with previous data, and the new data do not significantly alter the Q^2 scaling function used here (eq. 20, derived from the older data sets.

The unseparated cross sections are plotted as a function of ϵ in Figures 14 and 15. A linear least-squares fit was performed at each value of Q^2 to determine the best straight line ($\sigma = \sigma_T + \epsilon\sigma_L$) through the points. The resulting values of σ_L, σ_T, and $R = \sigma_L/\sigma_T$ are shown in Table V. Although only statistical and random systematic errors were used in the linear fit, the errors on

Λ channel

$\langle Q^2\rangle$ GeV^2	$\langle W\rangle$ GeV	$-t_{min}$ (GeV)^2	ϵ	$\sigma_T + \epsilon\sigma_L$ nb/sr
0.52	1.84	0.22	0.552	369.2 ± 12.1
			0.771	380.2 ± 12.2
			0.865	395.3 ± 12.5
0.75	1.84	0.30	0.462	346.3 ± 11.8
			0.724	362.8 ± 10.9
			0.834	379.2 ± 11.2
1.00	1.81	0.41	0.380	320.0 ± 10.7
			0.678	343.3 ± 10.7
			0.810	344.8 ± 11.6
2.00	1.84	0.74	0.363	221.8 ± 9.0
			0.476	233.4 ± 8.9
			0.613	237.7 ± 7.9

Σ^0 channel

$\langle Q^2\rangle$ GeV^2	$\langle W\rangle$ GeV	$-t_{min}$ (GeV)^2	ϵ	$\sigma_T + \epsilon\sigma_L$ nb/sr
0.52	1.84	0.31	0.545	70.1 ± 4.0
			0.757	86.5 ± 4.8
			0.851	91.4 ± 5.0
0.75	1.84	0.41	0.456	55.1 ± 3.2
			0.709	65.8 ± 4.0
			0.822	67.6 ± 4.1
1.00	1.81	0.55	0.375	37.2 ± 2.1
			0.663	44.4 ± 2.7
			0.792	47.3 ± 2.8
2.00	1.84	0.95	0.352	22.7 ± 1.5
			0.461	21.7 ± 1.4
			0.598	24.7 ± 1.5

TABLE IV: Results for the unseparated p(e,e′K$^+$)Λ and p(e,e′K$^+$)Σ^0 cross sections used in the L/T separation (i.e., not including an overall systematic error of 5%). The data have been scaled to $\theta^*_{qK} = 0^\circ$ and to the W and Q^2 values in the table, using the procedure outlined in section IV.C. Note that because a single experimental setting was used to acquire both Λ and Σ^0 data, the results are at different values of $-t_{min}$ for fixed θ^*_{qK}.

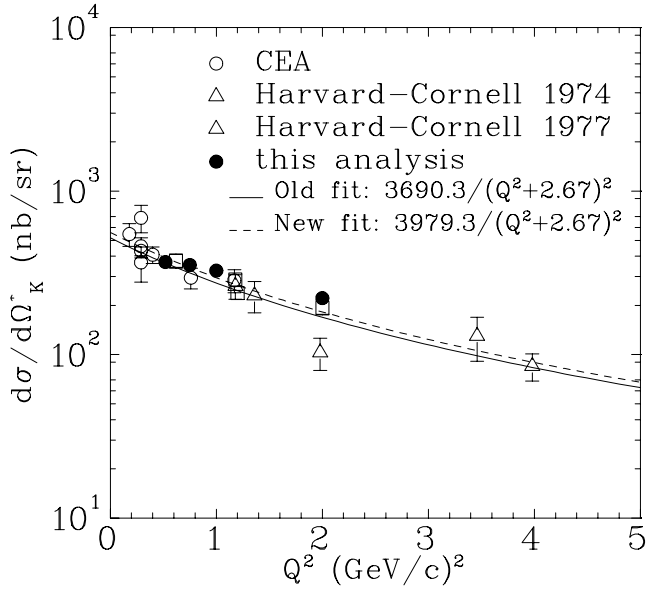

FIG. 12: Previous world data with the addition of the high-ϵ results of this analysis (solid points) scaled to $\langle W\rangle = 2.15$ GeV, $\theta^*_{qK} = 0°$, for the p(e,e′K$^+$)Λ unseparated cross sections. The "new fit" includes the results of this analysis.

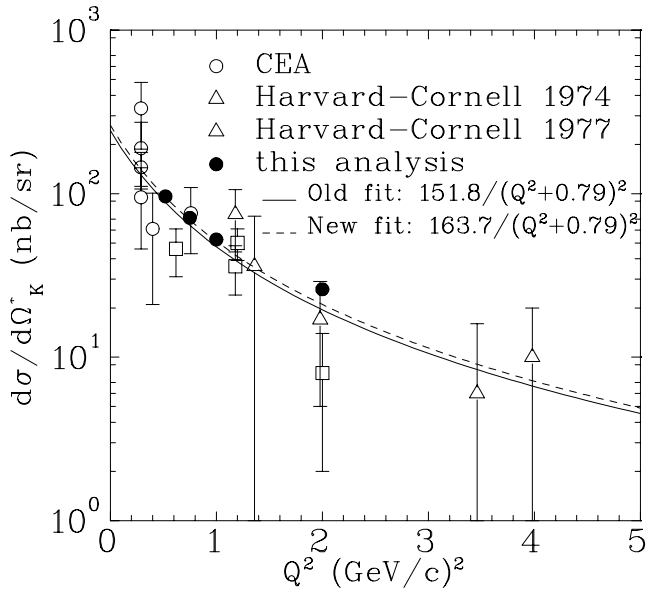

FIG. 13: Previous world data with the addition of the high-ϵ results of this analysis (solid points) scaled to $\langle W\rangle = 2.15$ GeV, $\theta^*_{qK} = 0°$, for the p(e,e′K$^+$)Σ^0 unseparated cross sections. The "new fit" includes the results of this analysis.

the extracted values of σ_L and σ_T include the scale errors added in quadrature with the random errors. The quantity R is insensitive to scale errors.

The separated cross sections σ_L and σ_T for the Λ channel are plotted as a function of Q^2 in Figures 16(a) and 16(b), respectively, along with other existing data.

Λ channel

$\langle Q^2\rangle$	$\langle W\rangle$	σ_L (nb/sr)	σ_T (nb/sr)	R = σ_L/σ_T
0.52	1.84	77.0 ± 53.9	325.4 ± 42.8	0.24 ± 0.17
0.75	1.84	83.9 ± 42.9	306.2 ± 33.5	0.27 ± 0.14
1.00	1.81	62.1 ± 35.4	297.5 ± 26.9	0.21 ± 0.12
2.00	1.84	61.4 ± 47.6	201.1 ± 26.0	0.31 ± 0.24

Σ^0 channel

$\langle Q^2\rangle$	$\langle W\rangle$	σ_L (nb/sr)	σ_T (nb/sr)	R = σ_L/σ_T
0.52	1.84	71.6 ± 20.2	31.3 ± 14.0	2.29 ± 1.20
0.75	1.84	36.1 ± 13.6	38.9 ± 9.0	0.93 ± 0.40
1.00	1.81	24.4 ± 8.1	28.1 ± 5.0	0.87 ± 0.32
2.00	1.84	8.4 ± 8.5	19.0 ± 4.2	0.44 ± 0.46

Ratio of Σ^0 / Λ

$\langle Q^2\rangle$	$\langle W\rangle$	$\sigma_L(\Sigma^0)/\sigma_L(\Lambda)$	$\sigma_T(\Sigma^0)/\sigma_T(\Lambda)$
0.52	1.84	0.929 ± 0.702	0.096 ± 0.045
0.75	1.84	0.431 ± 0.274	0.127 ± 0.033
1.00	1.81	0.393 ± 0.259	0.094 ± 0.019
2.00	1.84	0.136 ± 0.175	0.095 ± 0.024

TABLE V: L/T separated cross section results from this analysis for reactions p(e,e′K$^+$)Λ and p(e,e′K$^+$)Σ^0, and for the ratio of Σ^0 to Λ cross sections.

The equivalent plots for the Σ^0 channel are in figure 17. Photoproduction points from [29] are also shown in the transverse components, taken at comparable values of W and $\theta^*_{qK} \sim 30°$. For these figures they are scaled (corresponding to an upward adjustment of 1.3 (1.1) for Λ (Σ^0)) to $\langle W\rangle = 1.84$ GeV, $\theta^*_{qK} = 0°$ to yield (390 ±18) nb/sr. The third panel of each plot contains the ratio $R = \sigma_L/\sigma_T$ as a function of Q^2, along with data from [3]. The curves shown are from the WJC model [5] and from the unitary isobar model KAONMAID with its default parameterizations [6].

Finally, the ratio of Σ^0/Λ separated cross sections σ_L and σ_T are shown plotted vs. Q^2 in Figures 18(a) and 18(b), respectively, along with curves from the two models.

It should be noted that the data for E93-018 were taken in parallel with another experiment, E91-016 [30], in which angular distributions of kaon electroproduction from hydrogen and deuterium were studied. In a few cases the kinematic settings were very similar, and comparisons were made with cross sections extracted from two additional independent analyses of the Λ channel [26, 31]. They are in excellent agreement (within 2.5%), particularly when they are scaled to the same Q^2 and W using the equations 20 [3] and 22 [26] as described above.

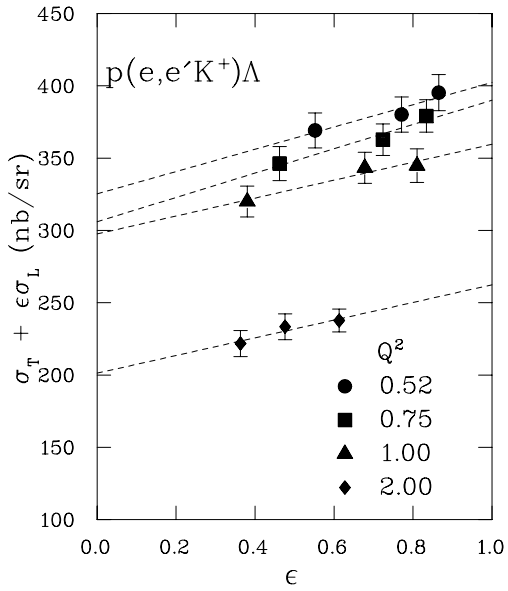

FIG. 14: Cross sections as a function of ϵ for p(e,e′K$^+$)Λ, shown with the linear fit to the data that allows separation into the longitudinal and transverse components.

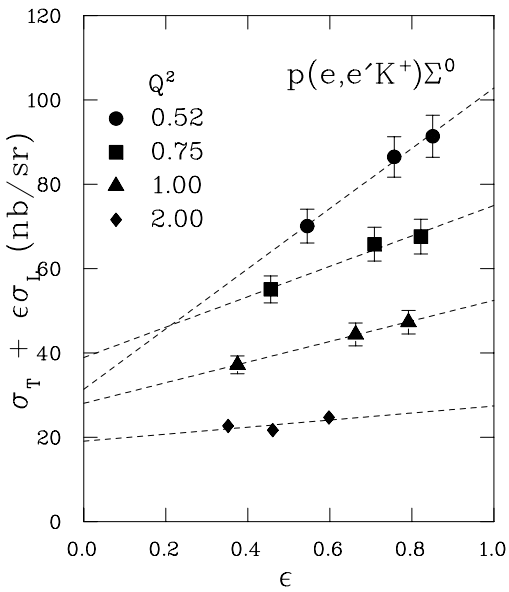

FIG. 15: Cross sections as a function of ϵ for p(e,e′K$^+$)Σ^0 process. The lines are the fit to the data, allowing separation of the longitudinal and transverse components.

B. Comparison with Calculations

As described in the introduction, several model calculations of Λ and Σ^0 electroproduction cross sections, using parameters fit to existing data, are available. We have chosen to compare our data to the models in [5] (WJC) and [6] (KAONMAID), for which calculations were readily available in the form in which the data are presented here. The parameters of each model are constrained by global fits to unpolarized photo- and electroproduction data, and, through crossing arguments, to kaon radiative capture.

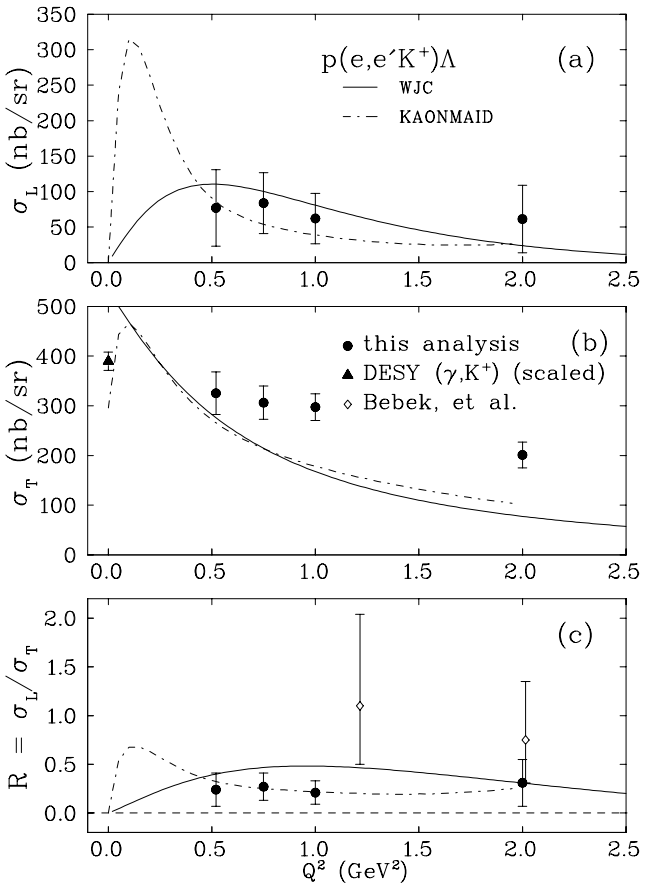

FIG. 16: Longitudinal (a) and transverse (b) cross sections for p(e,e′K$^+$)Λ as a function of Q^2. The ratio is shown in panel (c). The data are compared to calculations of [5] (solid line) and [6] (dot-dashed line).

For the Λ channel, both models generally reproduce the behavior of the longitudinal part of the cross section (Figure 16(a)), but underestimate the transverse component (Figure 16(b)) and thus overestimate the ratio $R = \sigma_L/\sigma_T$. One possible cause for the discrepancy could be the lack of knowledge of the Q^2 dependence of the baryonic form factors entering in the s-channel[32]. Very little data exist from which form factors for strange baryons can be extracted. In their study of kaon electroproduction, David *et al.*, observed that σ_L/σ_T was sensitively dependent on the choice of baryon form factors, while rather insensitive to the reaction mechanism [9], whereas the unpolarized cross section alone did not depend strongly on the baryon form factors.

For p(e, e′K$^+$)Σ^0, the WJC model reproduces reasonably well the trends of the data in both the longitudinal and transverse channel (Figures 17(a) and 17(b), respectively). As a result it also shows the proper trend in the ratio $R = \sigma_L/\sigma_T$ (Figure 17(c)) with the exception of the strong peak in R at low momentum transfer

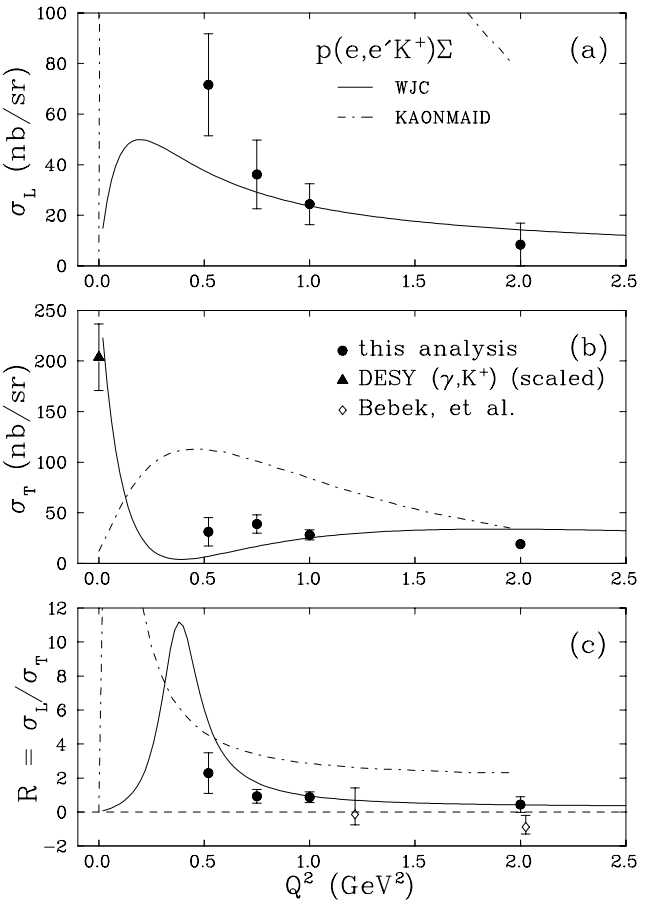

FIG. 17: Longitudinal (a) and transverse (b) cross sections for p(e,e′K$^+$)Σ^0 as a function of Q^2. The ratio is shown in panel (c). The calculations are again from [5] (solid line) and [6] (dot-dashed line).

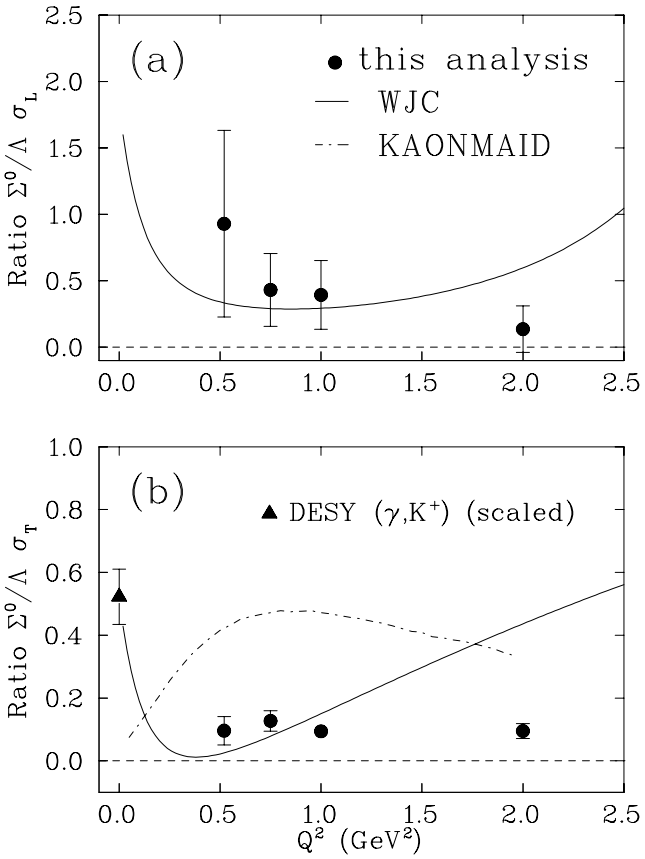

FIG. 18: Ratio of Σ^0/Λ cross sections as a function of Q^2, separated into longitudinal (a) and transverse (b) components, compared with the same two calculations as above. The KAONMAID calculation does not appear in (a) because it is an order of magnitude too large compared with the data.

that is not implied by our data. The magnitude of this peak in the WJC model is very sensitive to the CM energy, W, of the reaction, indicating that there are strong resonance contributions in the model. As in the case of the Λ channel, it is likely that the form factors and the strengths of the various resonances entering the model could be modified in order to give better agreement with the data. In general, the model for the Σ^0 is harder to tune than for the Λ because of the influence of isovector Δ resonances (of spin 1/2 and 3/2 in the model) in the Σ^0 channel.

The KAONMAID calculation somewhat overpredicts the transverse component of the Σ^0 channel, and overpredicts the longitudinal one by an order of magnitude. In KAONMAID, the strength of σ_L appears to come entirely from the P11(1710) resonance, which in this model has a large longitudinal form factor [33]. If this resonance is removed from the calculation, KAONMAID significantly underpredicts σ_L for both the Λ and Σ^0 channels.

The ratio of the longitudinal cross sections for Σ^0/Λ (Figure 18(a)) appears to show a decrease with increasing Q^2. This could arise from a decrease in the ratio of $g_{\Sigma NK}/g_{\Lambda NK}$ with increasing Q^2.

We note that while Regge trajectory models are not expected to work well at the rather low CM energy of our data, which are still within the nucleon resonance region, our highest Q^2 results are in reasonable agreement with the calculation of [34], both in the unseparated cross sections and in the L/T components. At lower momentum transfer our data indicate a signficantly larger longitudinal component to the Σ^0 cross sections than predicted by their model, perhaps indicative of the larger number of resonance contributions to the Σ^0 channel.

The ratio of the transverse cross sections for Σ^0/Λ (Figure 18(b)) does not show any appreciable decrease above $Q^2 \approx 0.52$ GeV^2. However, the inclusion of the DESY photoproduction data on the plot shows that there is likely a rapid decrease in the R_T for Q^2 below 0.5 (GeV/c)^2. This lower momentum region may be of interest for further study, particularly in the Σ^0 channel.

Conclusions

Precise Rosenbluth separated kaon electroproduction data in two hyperon channels, p(e,e′K$^+$)Λ and p(e,e′K$^+$)Σ^0, have been presented. These results are the most precise measurements of the separated cross sections σ_T and σ_L made to date, particularly for the Σ^0 channel, and will help constrain theoretical models of these electroproduction processes. Comparison of isobaric models to the results can yield information about the coupling strengths of contributing resonances within the framework of the model as well as information about the form factors and off-shell vertex corrections entering the diagrams. These data can also be used in conjunction with other models to learn more about the reaction dynamics.

Acknowledgements

This work was supported by the Department of Energy and the National Science Foundation.

[1] G. Niculescu *et al.*, Phys. Rev. Lett. **81**, 1805 (1998).
[2] See, for example, JLab experiments E89-004 (R. Schumacher), E89-043 (L. Dennis), E93-030 (K. Hicks), E99-006 and E00-112 (D. Carman), and E98-108 (P. Markowitz, contact).
[3] C. J.Bebek *et al.*, Phys. Rev. **D15**, 3082 (1977).
[4] P. Brauel *et al.*, Z. Phys. **C3**, 101 (1979).
[5] R. A. Williams, C.-R. Ji, and S. R. Cotanch, Phys. Rev. **C46**, 1617, (1992).
[6] T. Mart and C. Bennhold, Phys. Rev. **C61**, 012201(R) (2000).
[7] M.Q. Tran *et al.*, SAPHIR collaboration, Phys. Lett. **B445**, 20 (1998).
[8] S. R. Cotanch, R. A. Williams, and C.-R. Ji, Physica Scripta **48**, 217 (1993).
[9] J. C. David, G. Fayard, G. H. Lamot, and B. Saghai, Phys. Rev. **C53** , 2613 (1996).
[10] R. Adelseck and B. Saghai, Phys. Rev. **C 42**, 108 (1990).
[11] T. Mart, C. Bennhold, and C. E. Hyde-Wright, Phys. Rev. **C51**, R1074 (1995).
[12] P. D. B. Collins, *An Introduction to Regge Theory and High Energy Physics*, (Cambridge University Press, Cambridge, 1977).
[13] M. Vanderhaegen, M. Guidal, and J.-M. Laget, Phys. Rev. **C57**, 1454 (1998).
[14] M. Guidal, J.-M. Laget, and M. Vanderhaegen, Nucl. Phys. **A627**, 645 (1997).
[15] J. Volmer *et al.*, Phys. Rev. Lett. **86**, 1713 (2001).
[16] Jefferson Laboratory experiment E98-108 (P. Markowitz, contact).
[17] J. Cleymans and F. Close, Nucl. Phys. **B85**, 429 (1975).
[18] O. Nachtmann, Nucl. Phys. **B74**, 422 (1974).
[19] R. C. E. Devenish and D. H. Lyth, Phys. Rev. **D5** 47 (1972).
[20] Particle Data Group, D.E. Groom*et al.*, European Physical Journal **C15**, 1 (2000).
[21] R. M. Mohring, Ph.D. thesis, University of Maryland (1999), (unpublished).
[22] N. C. R. Makins, Ph.D. thesis, Massachusetts Institute of Technology (1994), (unpublished).
[23] Y. S. Tsai, Phys. Rev. **122**, 1898 (1961), L. M. Mo and Y. S. Tsai, Rev. Mod. Phys. **41**, 205 (1969).
[24] T. G. O'Neill, Ph.D. thesis, California Institute of Technology (1994), (unpublished).
[25] C. S. Armstrong, Ph.D. thesis, College of William & Mary (1999), (unpublished).
[26] D. M. Koltenuk, Ph.D. thesis, University of Pennsylvania (1999), (unpublished).
[27] C. J. Bebek *et al.*, Phys. Rev. **D 15**, 594 (1977).
[28] C. N. Brown *et al.*, Phys. Rev. Lett. **28**, 1086 (1972).
[29] P. Feller *et al.*, Nucl. Phys. **B39**, 413 (1972).
[30] B. Zeidman, JLAB proposal E91-016 (unpublished) (1991).
[31] J. Cha, Ph.D. thesis, Hampton University (2001), (unpublished).
[32] S. R. Cotanch, private communication (1999).
[33] C. Bennhold, private communication (2001).
[34] M. Guidal, J.-M. Laget, and M. Vanderhaegen, Phys. Rev. **C61**, 025204 (2000).